Study of Polyoxometalates as Electrode Materials for Lithium-Ion Batteries: Thermal Stability Paves the Way to Improved Cycle Stability

Georg-Maximilian Bosch,[a, b] Angelina Sarapulova,[b] and Sonia Dsoke*[a, b]

Polyoxometallates (POMs) are ideal candidates for energy storage because of their multi-electron transfer. $(n\text{-}Bu_4N)_3PW_{12}O_{40}$ (TBA-PW) and $Cs_3PW_{12}O_{40}$ (Cs-PW), prepared by proton-exchange with tetrabutylammonium (TBA^+) and cesium (Cs^+) from $H_3PW_{12}O_{40}$, suffer from serious capacity fading, owing to the contained crystal water. The presence of water in POMs is well known, but its effect on electrochemical performance is not reported yet. In contrast to TBA-PW, Cs-PW has a higher thermal stability and can be treated at 600 °C, which allows the complete water removal (Cs-PW-600). Cs-PW-600 has a 15-times better cycling performance than the one dried at 120 °C. Different pressures were applied to optimize the electrode fabrication. Samples treated at 8 tons show a three-times better rate capability with respect to the unpressed sample, with 42.8% retention of the capacity at 200 mA g^{-1}. Cs-PW-600 can be seen as an example for further investigations on POMs as electrode materials.

1. Introduction

Along with the development and usage of renewable energies all over the world, high energy density and fast-charging batteries, in particular, lithium-ion batteries (LIBs), are playing an important role, replacing fossil energy sources.[1] However, the realization of this replacement in large scale energy storage is strongly limited by high cost, low abundance resources of elements like cobalt (which is contained in most commercial active materials).[2–4] It is, therefore, urgent to develop new alternative electrode materials beyond the classic ones to meet the increasing demand for high power density and energy density.[5]

Polyoxometalates (POMs) have been widely investigated in many different areas, such as catalysis,[6] anti-bacterial products,[7] water-splitting,[8,9] synthesis of organic compounds,[10] and energy conversion.[11–13] POMs show excellent stability against reduction and oxidation and can absorb and release up to 24 electrons in fast and reversible one- or multi-electron reactions. They are called "electron sponges"[14,15] and considered as ideal candidates for electrode materials. Moreover, POMs are widely used as salt for aqueous electrolyte in their acidic form due to their good solubility of ~0.8 M in water at 25 °C.[16–18] The molecule-like POM units, also can be combined with different high surface area supporting materials as hybrid material, which can overcome the high solubility and increase the electronic conductivity.[11] Further, different types of POMs can be combined in a mixed material which can show pseudocapacitive behavior.[19] These molecular-like polyatomic anions consist of three or more transition metal oxyanions ($M_xO_y^{z-}$), which usually belong to group 5 or group 6 elements.[20] They form a large and closed 3-dimensional framework by sharing oxygen atoms, which is seen as their primary structure and also called cluster. The crystal structures, built out of these clusters, often includes a considerable amount of bounded water between the clusters, acting as a kind of bridge between them.[21,22]

The Keggin-type ($[XM_{12}O_{40}]^{n-}$, $X = P^{5+}$, Si^{4+}, B^{3+}; $M = Mo^{6+}$, W^{6+}) is one of the best known POM structures, which is also often used in aqueous-based electrochemical storage systems.[23] Among them, phosphotungstic acid $H_3PW_{12}O_{40}$ (H-PW) is one of the most stable.[24]

Nevertheless, H-PW is rarely used as electrode material in organic-based electrochemical energy storage systems because of its high solubility in most of the organic-based electrolytes used in LIBs.

It is well-know the method to exchange the protons by other cations, such as tetrabutylammonium (TBA^+) and cesium (Cs^+), to obtain an insoluble POM-based material, like $(n\text{-}Bu_4N)_3PMo_{12}O_{40}$ (TBA-PMo) and $Cs_3PW_{12}O_{40}$ (Cs-PW) and also to increase the thermal stability.[25–30] For example, Wang *et al.* reported a TBA-PMo electrode, made of 10% of active material in the electrode mixture. Its large discharge capacity of 270 mAh g^{-1} (only two cycles are reported) was correlated to the electrochemical reduction of all 12 Mo^{6+} ions to Mo^{4+} in the discharging process, revealed by *in operando* X-ray absorption spectroscopy (XAS).[14] During the first lithiation, a reduction of the metal centres occurs and the whole cluster is negatively charged. As shown in the chemical reaction (1) this charge is balanced by the addition of a

[a] G.-M. Bosch, Dr. S. Dsoke
Helmholtz-Institute Ulm for Electrochemical Energy Storage (HIU)
P.O. Box 3640, Karlsruhe, Germany
[b] G.-M. Bosch, Dr. A. Sarapulova, Dr. S. Dsoke
Institute for Applied Materials – Energy Storage Systems (IAM-ESS)
Karlsruhe Institute of Technology (KIT)
76344 Eggenstein-Leopoldshafen, Germany
E-mail: sonia.dsoke@kit.edu

Supporting information for this article is available on the WWW under https://doi.org/10.1002/celc.202001451

positively charged lithium ion and it can be repeated up to 24-times.[14]

$$\left[PW_{12}^{VI}O_{40}\right]^{3-} + n\cdot e^{-} + n\cdot Li^{+} \rightleftharpoons \left[Li_nPW_{12}^{\left(VI-\frac{n}{12}\right)}O_{40}\right]^{3-} \quad (1)$$

It is assumed that the lithium ions either accumulate in the interstices or on the surface of the POM cluster,[31] or the lithium ions penetrate directly into the cluster.[32] In the case of delithiation, the process takes place in reverse order. However, POMs contain crystal water. It is known that residual water can lead to serious side reactions in a typical organic electrolyte for LIBs (e.g. $LiPF_6$ in EC/DMC) and thus is harmful to cycle stability.[33] Nevertheless, the influence of crystal water of POM structure on the electrochemical performance and stability in organic-based LIBs is still unclear. To the best of our knowledge, there is no work focusing on phosphotungstic oxide as electrode material in organic electrolyte.

In addition, organic TBA^+ based POM suffers from serious thermal stability problems due to the decomposition at high temperatures during drying.[34] This problem can be overcome by using inorganic Cs^+ as precipitation agent instead.[30,35–39]

This work aims to investigate the electrochemical performance of phosphotungstic oxide based materials as the most stable Keggin-type POM and to improve its cycling stability. For this purpose insoluble $(n\text{-}Bu_4N)_3PW_{12}O_{40}$ (TBA-PW) and Cs-PW were synthesized and treated at different temperatures. The materials are analyzed by thermogravimetric analysis (TGA), *in situ* high-temperature powder X-ray diffraction (HT-XRD), and scanning electron microscopy (SEM). Furthermore, the water content and its influence on the cycle stability is investigated.

2. Results and Discussion

2.1. Improvement of Cycle Stability

In this work, the materials dried at 120 °C under vacuum for 12 h are defined as standard ones, marked as TBA-PW-120 and Cs-PW-120 for TBA-PW and Cs-PW, respectively.

Figure 1a and 1b show the cyclic voltammogram (CV) of TBA-PW-120 and Cs-PW-120 at a scan rate of 1 mV s^{-1} in the potential range of 1.4–3.5 V *vs.* Li/Li$^+$, respectively. TBA-PW-120 (Figure 1a) in the first cycle, shows five distinct and separate redox peak couples (Delitiation/Lithiation) at (I) 1.62/1.55, (II) 1.79/1.75, (III) 2.23/2.14, (IV) 2.47/2.42 and (V) 2.75/2.71 V. The peaks II_{Li}, III_{Li}, III_{Deli}, and IV_{Li} show some small shoulders, indicating an overlap of various single and multiple electron reactions. Along with repeated scanning, there is a significant decrease in the intensities of all peaks starting with a capacity of 16.41 mAh g^{-1} in cycle one, to almost no distinct peaks after 30 scans.

Compared with TBA-PW-120, Cs-PW-120 shows four broad and overlapped reversible redox peaks with a higher current intensity of the peaks especially around 1.6 V ($I + II_{Deli}$) for the first scan, indicating different reaction processes from that of TBA-PW-120. After four cycles the redox waves of Cs-PW-120 split into seven redox waves at (Deli/Li) (I) 1.67/1.48, (II) 1.82/1.7, (III) 2.17/2.02, (IVa) 2.42/2.21, (IVb) 2.5/2.29, (Va) 2.67/2.29, (Vb) 2.75/2.67 V. Unfortunately, Cs-PW-120 also displays a fast capacity decrease with 48.48 mAh g^{-1} in the first cycle and almost no visible redox peaks after 30 cycles. Interestingly, the electrochemical behavior of both phosphotungstic oxide materials is similar to that observed for H-PW-based materials in aqueous system reported by Martel *et al.*.[40] Although the intensity of the current and the capacity has changed after the exchange of the cations, the fast decrease of the capacity for both materials seems not to depend on the cation TBA^+ or Cs^+. It can be assumed that a common cause leads to a deactivation or degradation of the active materials.

Since the presence of crystal water in host materials could cause a poor cycling stability,[33] TGA was carried out to reveal the amount of water contained in the material, and to study

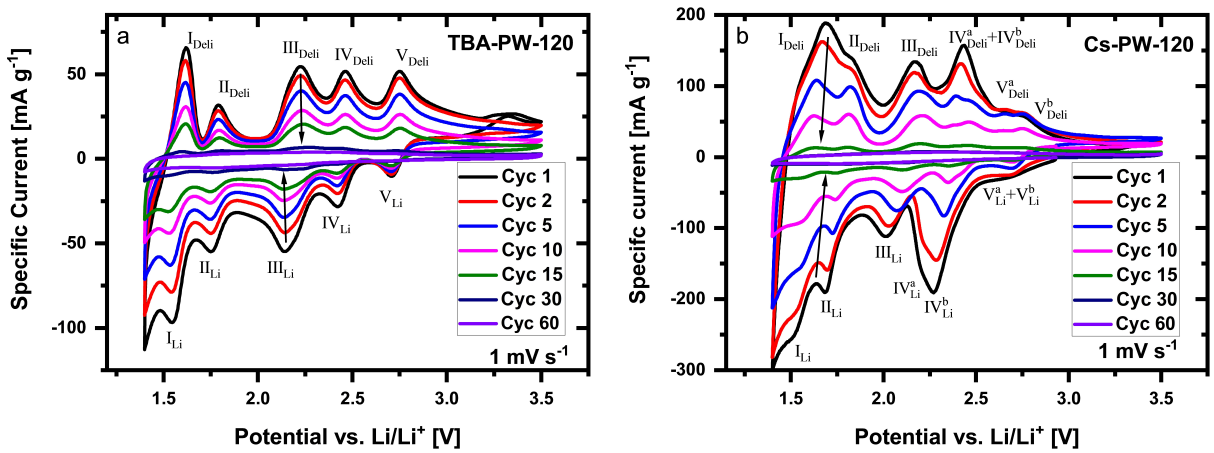

Figure 1. CV of TBA-PW-120 (a) and Cs-PW-120 (b) at 1 mV s^{-1}.

the thermal stability. TGA of TBA-PW-120 in Figure 2a shows a weight loss of around 1.4% at 225 °C, which is primarily attributed to the surface absorbed or weak bound water. The weight loss of around 20.5% above 300 °C is related to the decomposition of the organic $(n\text{-}Bu_4N)^+$-part. Above 600 °C, no further decomposition or weight loss can be observed. The residual mass of 78.1% refers to the amount of remaining inorganic POM. In contrast, TGA of Cs-PW-120 displays a weight loss of around 2.5% between 100–150 °C, which can be attributed to adsorbed, weak bound water. A weight loss of only 0.5% between 350–600 °C is related to the loss of crystal water from the material. Above 600 °C, no further weight loss is observed and the material remains stable up to 800 °C.

In situ HT-XRD (Figure 3a) patterns are collected from room temperature (RT) up to 800 °C with steps of 200 °C and finally returning back to RT, using the same heating rate as in TGA (Figure 2). The reflections of Cs-PW-120 gradually shift to low angles and their intensities increase along with the increase of the temperature to 800 °C, indicating a very stable crystal structure. A calculation of the particle size (by Debye-Scherrer

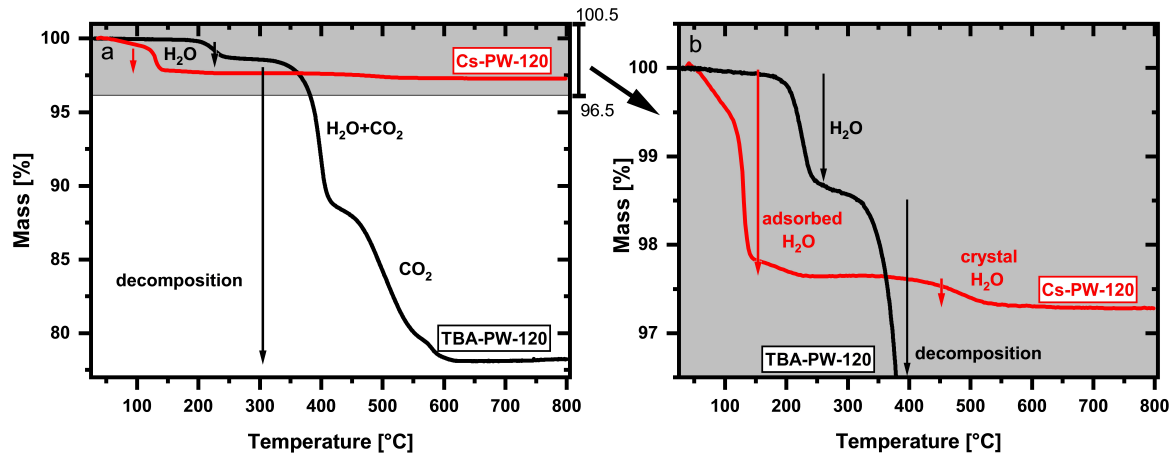

Figure 2. a) TGA of TBA-PW-120 (black) and Cs-PW-120 (red); b) enlarged shaded region of (a).

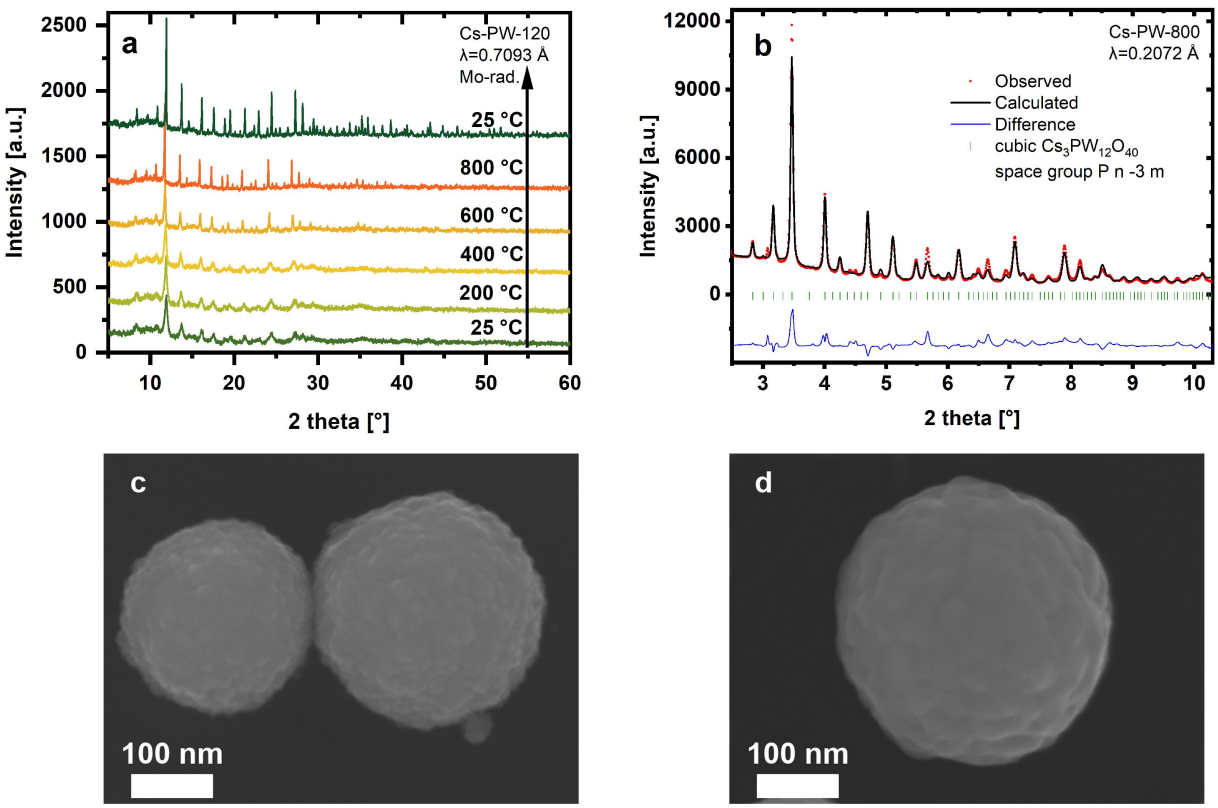

Figure 3. a) High-temperature XRD diffraction pattern of $Cs_3PW_{12}O_{40}$ between RT and 800 °C and RT, b) refinement of XRD pattern after heat treatment. SEM: aggregate of c) Cs-PW-120 and d) Cs-PW-600 primary particles.

equation) from the simulated XRD pattern by Rietveld method revealed a size of around 10 nm for the pristine and a size of 20 nm for the treated particles at 600 °C; therefore agglomeration and crystal growth with increasing the temperature can be assumed.

Figure 3b shows the fitting of the XRD pattern with the theoretical one by the Rietveld method. The pattern was collected at synchrotron PETRA III from Cs-PW sample after heat-treatment at 800 °C (Cs-PW-800) and proofs the stability of the crystal strucutre.

In Figure 3c and 3d SEM pictures of Cs-PW-120 and Cs-PW-600 particles are shown. In agreement with XRD, the primary particles of the pristine and treated sample are around 10 nm and 50 nm, respectively. These primary particles aggregate to spheric secondary particles of 200 to 250 nm, respectively.

As displayed in Figure 1, both TBA-PW-120 and Cs-PW-120 suffer from serious capacity fading, which might be related to the crystal water in the materials. Considering the informations obtained from the TGA (Figure 2), 600 °C was chosen as a suitable and sufficient treatment temperature for drying Cs-PW, marked as Cs-PW-600, also, with regard to environmental aspects.

The CV profile of Cs-PW-600 in Figure 4a shows five peak pairs at (Deli/Li) (I) 1.75/1.41, (II) 1.9/1.58, (III) 2.13/1.84, (IVa) 2.36/2.07, (IVb) 2.46/2.24 V, which have a similar shape like Cs-PW-120 but with higher polarization. The initial current intensity of the peaks III, Va and Vb is lower than that for Cs-PW-120, whereas the current intensity of peak I, II, IVa and IVb is comparable to the peaks of Cs-PW-120. Compared with Cs-PW-120, the cycling stability of Cs-PW-600 has been significantly improved. After 30 cycles the redox reactions are well visible and even after 60 cycles, only a small decrease of current intensity is observed.

Figure 4b shows the specific capacity of the three materials TBA-PW-120, Cs-PW-120, and Cs-PW-600 calculated from their CV during cycling. TBA-PW-120, Cs-PW-120, and Cs-PW-600 have an initial capacity of 36.8, 46.1, and 36.5 mAh g^{-1}, respectively. During the first 15 cycles, TBA-PW-120, Cs-PW-120 show poor cycling stability with a fast decrease of capacity and poor efficiency. In contrast, Cs-PW-600 shows improved cycling stability. From the second cycle onwards, the efficiency of Cs-PW-600 is close to 100 % and the capacity is more and more stabilizing.

In total, the material has a low specific capacity, which is due to the high molecular weight of the cluster and also due to the partial redox reaction in the materials. However, it should be emphasized that the cycling stability has been improved by at least 15-times. This result can open the way to other analogs low-weight and high energy POM-type materials.

2.1.1. Post Mortem Characterization

It is well known that some irreversible side reactions can occur in LIBs in the presence of water molecules and residues can, for example, form a surface layer.[33] SEM was used to study the morphology change of the pristine and the cycled electrode after 60 cycles. SEM images of Cs-PW-120 and Cs-PW-600 powder, shown in Figure 3c and 3d reveal spherical particles with a size of 200 to 250 nm. These particles also can be seen on the pristine electrodes in Figure 5a and 5b. Furthermore, *post mortem* analysis of the electrodes is shown in Figure 5c and 5d. The inlays of these pictures show the energy specific separation of backscattered electrons (ESB), where white areas show more heavy atoms, e.g. POMs and dark areas show lighter ones, e.g. organic compounds.

Cs-PW-120-based electrode (Figure 5c) shows many cavities on the surface and seems to consist of rather soft, bulky material. The inlay of Figure 5c is mostly black and shows only very faint white spots, indicating a low electron density of the atoms in the surface layer.

In comparison, individual and spherical POM particles can be recognized in Figure 5d. However, similar soft, bulky structures can be observed in some areas. The inlay of Figure 5d shows a good match with the SEM picture, where areas with particles appear white, and areas with the soft structure appear black.

After 60 cycles, the active material of Cs-PW-120 can be hardly detected on the surface of the electrode. This suggests

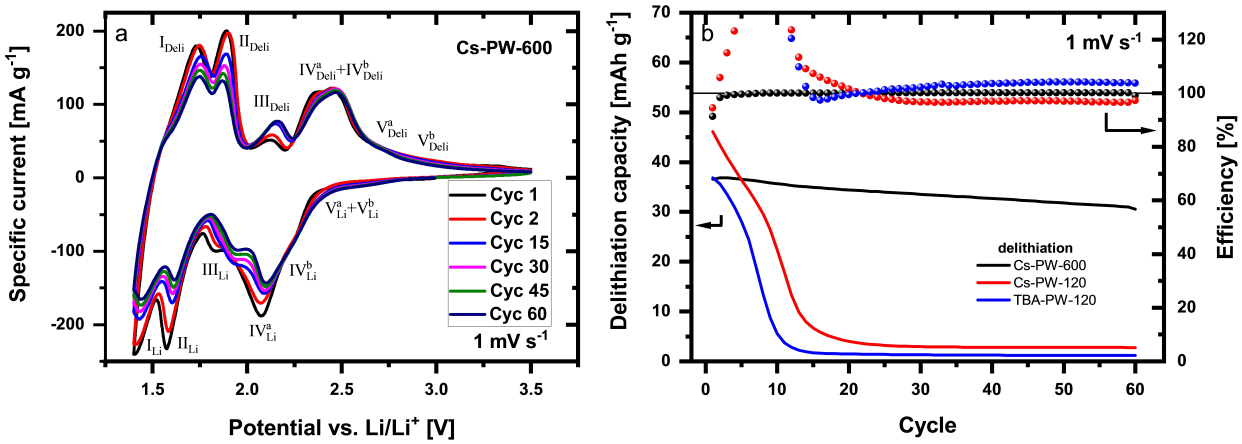

Figure 4. a) CV of Cs-PW-600 at 1 mV s^{-1} and b) specific capacity (lines) and efficiency (balls) vs. cycles of TBA-PW-120, Cs-PW-120 and Cs-PW-600 electrodes.

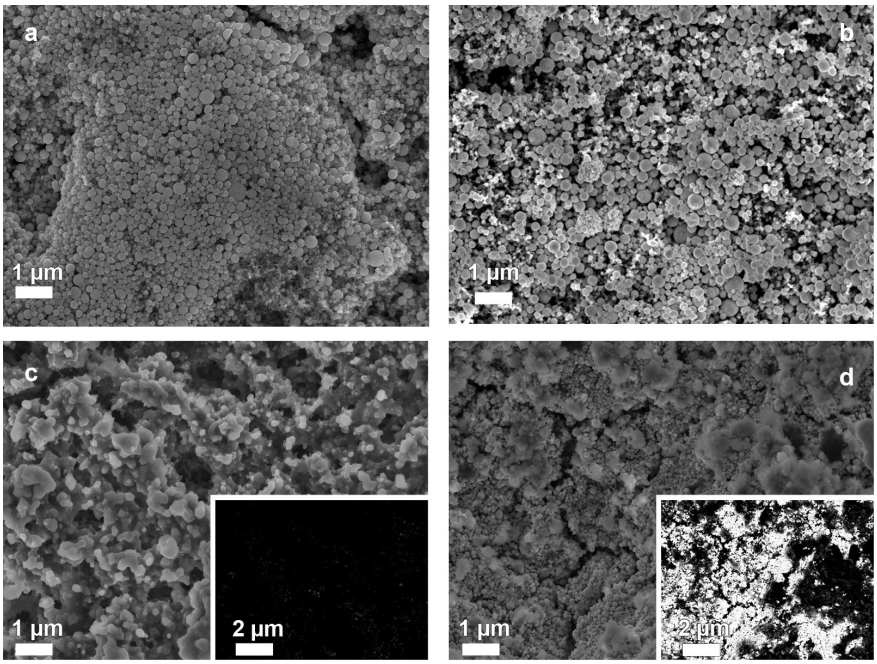

Figure 5. SEM pictures of electrode with Cs-PW-120 a) before and c) after cycling, and pictures of electrode with Cs-PW-600 b) before and d) after cycling; inlays of (c) and (d) show compositional contrast (ESB) of each SEM picture.

that the POM material is covered by an organic layer of decomposition products. Further, it can be seen that very less organic layer is detected on the surface of Cs-PW-600 sample. TGA in Figure 2 showed remaining water molecules in the structure of the untreated sample, which can cause side reactions. Therefore it can be inferred that the organic layer can be associated with the decrease in capacity, by blocking the path for lithium insertion.

2.2. Electrode Optimization and Electrochemical Investigation

Although the cycling stability of Cs-PW is improved by the heat-treatment at 600 °C, it still displays an unsatisfied electrochemical performance, in terms of polarization and current rate capability. It is well known that the electrochemical performance of a material is not only dependent on the material itself but also on the electrode fabrication.[41] Herein, it is necessary to optimize the electrode preparation to lower inner resistances and finally obtain a better rate capability.

To optimize the fabrication process of the electrode, further experiments were conducted with Cs-PW-600 electrodes by applying different pressures. The electrode pressed at 8 t is compared with the not pressed one by SEM and XRD (Figure 6). A morphological and structural change of the material can be excluded, as the POMs spherical particles still keep their integrity and XRD pattern are not changed. Nevertheless, it can be observed that the pressure causes a spatial approximation of the particles and the other components of the electrode. This fills the interstices and packs the electrode more tightly. The high force also causes some superficial particles to be flattened. The total thickness of the electrode was reduced from 33 µm to 31 µm after applying the pressure.

Figure 7a and 7b show each first CV cycle of Cs-PW-600 electrodes subjected to different pressures from 0 to 8 t. The complete series of CV profiles (over 60 cycles per electrode type) can be found in the supporting information (Figure S1). Depending on the pressure applied, the samples are labeled as Cs-PW-0 t to Cs-PW-8 t. Figure 7b1 and 7b2 show a magnification of the reaction peaks of I_{Deli} and IV_{Li}. With increased pressure, the delithiation- and lithiation-related peaks continuously shift to lower and higher potentials, respectively, indicating a reduced polarization. The rather broad peaks of Cs-PW-0 t become sharper and more intense with increasing pressure, especially in the low potential region. Due to the decreased polarization, one additional redox peak can be clearly observed at around 1.5 V in Figure 7a when the pressure is over 1 t. Figure 7c shows the development of the polarization (dE) of the two selected redox waves I and IV of Figure 7a, along with the applied pressure, where the values are calculated from the maxima of the corresponding redox peak pairs. At zero pressure, the polarization of reaction IV_{Li} is about 0.32 V. With increasing the pressure to 8 t, the polarization appears to exponentially decrease to 0.08 V. I_{Deli} also shows the same exponential decrease.

Figure 7d shows the rate capability of Cs-PW-600 after applying 0 t, 4 t and 8 t to the electrode from 5–200 mAh g^{-1}. The non-pressed electrode Cs-PW-0 t has an initial capacity of 56.2 mAh g^{-1} at 5 mA g^{-1} and a capacity of only 7.9 mAh g^{-1} at 200 mA g^{-1}. However, it delivers a reversible capacity of 45.2 mAh g^{-1} when the current returns back to 5 mA g^{-1}. Cs-PW-4 t and Cs-PW-8 t show a slightly higher initial capacity, which

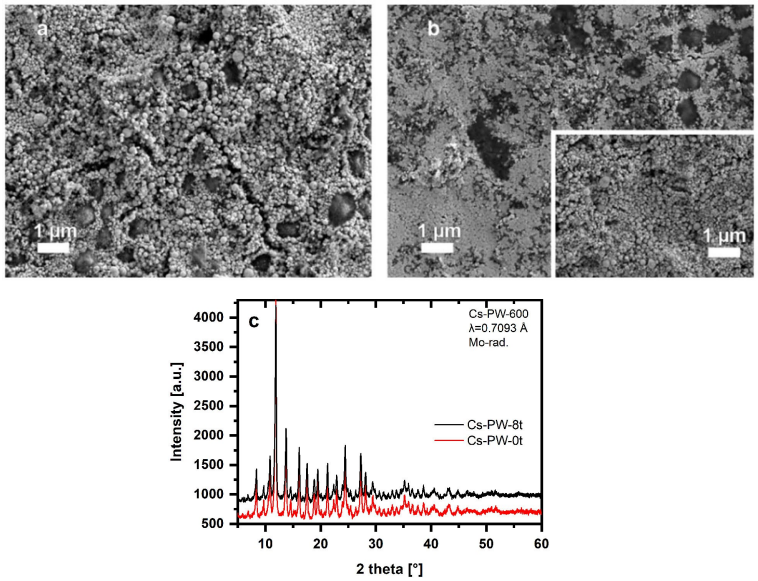

Figure 6. SEM pictures of Cs-PW-600 electrode after applying a) 0 t and b) 8 t pressure, and c) comparison of both by XRD.

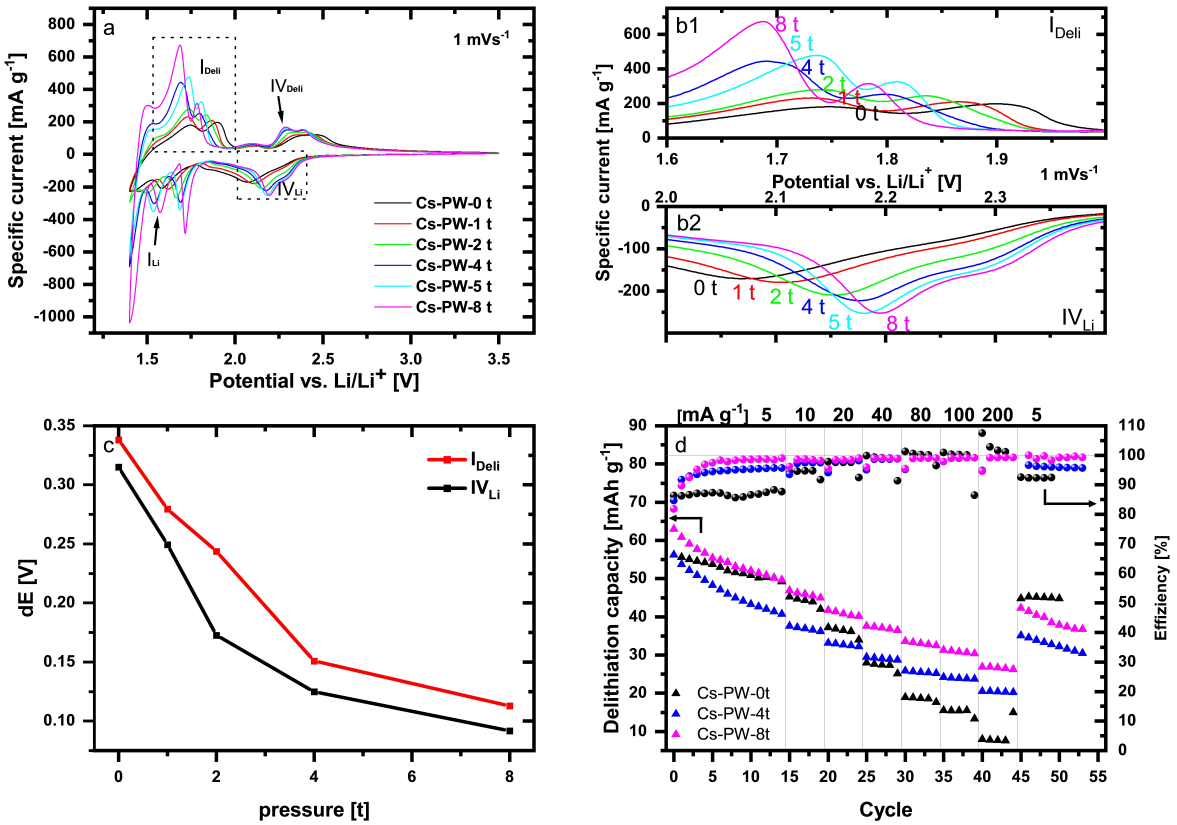

Figure 7. a) Cyclic voltammogram of pressed electrodes at 1 mV s^{-1}, b) magnification of peak I_{Deli} and IV_{Li}; c) reaction wave polarization and d) rate capability of $Cs_3PW_{12}O_{40}$ prepared at different pressures.

can be attributed to the new redox reaction at around 1.5 V. However, both of them decrease significantly fast in the first three cycles and have, before cylce 15 as well as after coming back to 5 mA g^{-1} a lower capacity than that of Cs-PW-0 t. Both Cs-PW-4 t and Cs-PW-8 t show a much higher capacity than that of Cs-PW-0 t when the current is higher than 20 mA g^{-1}. Cs-PW-0 t shows a capacity retention of 14% at 200 mA g^{-1}, while Cs-PW-4 t and Cs-PW-8 t display an improved one of 36.5% and 42.8%, respectively.

The applied pressure to the electrodes leads to a higher current intensity and more narrow peaks of Cs-PW-8 t (Figure 7a). This indicates a higher reaction speed. The shift of the redox peaks in Figure 7a and the shrinking polarization in Figure 7c can be attributed to reduced inner resistance of the electrode. This leads to a shift of a low-potential reaction inside the potential window, and to a higher initial capacity of the pressed samples (Figure 7d). The reason for the rapid decrease of the initial capacity of the pressed samples can be explained as follows: It can be assumed that the narrower pores become blocked in the first cycles and thus the accessability of active material and the capacity decreases. This should be confirmed by additional *post mortem* studies like SEM and/or porosity measurements on cycled electrodes, which is going beyond the scope of this work and it will be a topic of a future study. Nevertheless, the lower capacity of the Cs-PW-8 t electrode after 45 cycles (at 5 mA g^{-1}) compared to the unpressed sample can be explained by a progressive blocked diffusion of the electrolyte into the material and a shrunk active surface due to a too close packing of the electrode components, as it can be seen in Figure 6b. Nevertheless, the applied pressure enhances the contact between the particles, thus increasing the electronic conductivity. This leads to an improved reaction kinetics, a smaller polarization, and therefore, a better response to high currents for Cs-PW-4 t and Cs-PW-8 t in Figure 7d.

Since the two factors of electrical conductivity and accessibility of the electrolyte in the electrode work in opposite directions, the low contact of the untreated sample seems to have a smaller influence on the capacity at low currents than the reduced electrolyte accessibility of the pressed sample. Therefore, at low current, a higher capacity can be observed on the untreated sample. However, at higher currents, the influence of the improved contact of the particles prevails, which, compared to the untreated sample, leads to a better rate capability.

In order to address the variation of resistance with the pressure, the iR-drops of the galvanostatic cycles at 200 mA g^{-1} are compared (Figure 8). Clearly, the iR-drop and thus also the resistance decreases with increasing pressure. The largest change is observed from 0 t to 4 t, whereas only a very small change occurs from 4 t to 8 t. This is in good agreement with the trend of polarization displayed in Figure 7c.

In future studies, an optimum balance between particle contact and electrolyte accessibility will be tuned.

3. Conclusions

In this work, TBA-PW and Cs-PW were prepared by exchanging the protons with TBA^+ and Cs^+ from phosphotungstic acid. TGA demonstrates that TBA-PW-120 displays a significant decomposition of the organic $(n\text{-}Bu_4N)^+$-part and it is not suitable for drying at high temperatures, while Cs-PW-120 shows mass loss of crystal water from 350 to 600 °C. Both materials, TBA-PW-120 and Cs-PW-120 show a fast decrease in capacity during the first 15 cycles. After treatment at 600 °C, Cs-PW-600 shows a significant improvement of a 15-times higher

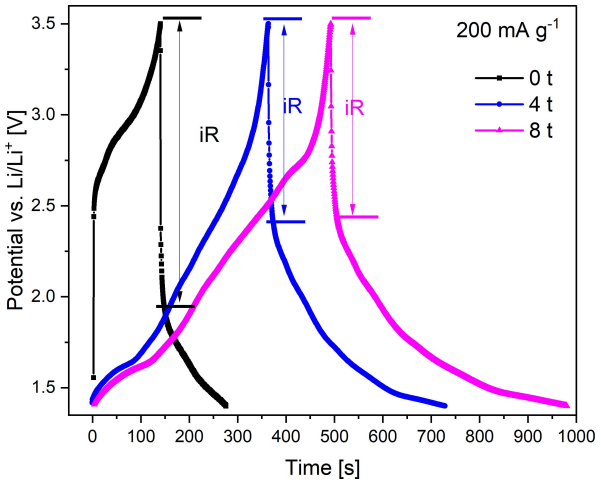

Figure 8. Comparison of GCPL curves at 200 mA g^{-1} of Cs-PW samples pressed at 0 t, 4 t and 8 t. iR-drop of each curve is highlighted to evaluate the variation of resistance with the pressure.

cycle stability with a capacity retention of 84.8 % after 60 cycles. Furthermore, *post mortem* studies demonstrate that side reactions in the untreated material lead to the formation of a layer of deposits on the electrode. This layer shields and deactivates the electrode from further reactions. After heat-treatment at 600 °C, these deposits can be minimized, where remaining crystal water is a major cause of these side reactions. Further investigations to minimize the polarization and the broadness of the reaction peaks show that pressing the electrode leads to three-times faster response to the applied current and four-times less polarization. By applying pressure to the electrode, it is possible to improve the contact between the particles. This minimizes the energy barrier and the inner resistance of the redox processes, and the faster reactions also lead to improved cycling behavior at higher currents.

Our investigations can be seen as a first and important step to open the way to further investigations on POMs as electrode materials in LIB and other typs of energy storage systems.

Experimental Section

(a) Material Synthesis

Heteropolytungstic acid ($H_3PW_{12}O_{40}{\cdot}xH_2O$) was obtained from Merck. Tetrabutylammonium chloride (TBA–Cl), poly(vinylidene fluoride) (PVDF) powder, lithium foil, and standard electrolyte LP30 was bought from Sigma-Aldrich. Cesium chloride (CsCl) were obtained from VWR. The conductive carbon black Super C65 was obtained from Timical. Porous glassy fibrous separator (GF/D, thickness 0.67 mm) were supplied by Whatman. Aluminum foil (thickness 15 μm) were obtained from Häberle. All chemicals were used without further purification. TBA-PW was synthesized by using previous published method.[29] Typically, 20 ml of 0.072 M TBA–Cl solution was added dropwise to 15 ml of 0.02 M H-PW solution with strong stirring. After 24 hours, when equilibrium was obtained, the precipitate was separated from the solution by centrifugation

and then washed with distilled water several times. The white powder was dried at 120 °C under vacuum for 24 h.

In the same way, Cs–W was synthesized by adding 10.5 ml of a 0.48 M CsCl solution dropwise to 25 ml of a 0.067 M H-PW solution while stirring to ensure a crystallization of monodisperse and small particles. After 30 minutes, the precipitate was separated from the solution by centrifugation and washed with distilled water several times. The white powder was dried at 120 °C under vacuum for 24 h. To get a water-free material, heat treatment was performed for Cs-PW-120 in a muffle furnace (Nabertherm P480) heating up at 600 °C for 4 h with a heating rate of 100 °C h^{-1} in air. After cooling down to RT, samples were stored under air.

(b) Material Characterization

TGA was performed on a Netzsch Jupiter 449 C between RT and 800 °C with a heating rate of 10 °C min^{-1} under an atmosphere mixed of 66 % argon and 34 % oxygen (5 mg material). Before each measurement, the empty crucible was heated up for baseline measurement. For TGA, loose of weight was recorded and the software Netzsch Proteus-Thermal Analysis was used to analyze the data. The decomposition products generated during heating, in parallel were analyzed by a coupled IR spectroscopy measurement.

In situ HT-XRD was performed on a Stoe X-ray diffractometer with molybdenum source (wavelength: 0.7093 Å, Mo-$K_{\alpha 1}$) to investigate the crystal structure of materials. The samples were measured in a 0.5 mm quartz capillary in a temperature range of 25–800 °C with steps of 200 °C with a heating rate of 10 °C min^{-1}. Additional *in situ* high-temperature XRD was performed using synchrotron radiation at PETRA-III beamline P02.1 at DESY in Hamburg, Germany ($\lambda = 0.2072$ Å). The samples were measured in a 0.5 mm quartz capillary in a temperature range of 25–800 °C with steps of 50 °C with a heating rate of 50 °C min^{-1}.

SEM was carried out on a ZEISS MERLIN scanning electron microscope to assess the morphology and particle size identification of particles.

(c) Electrochemical Characterization

The working electrode was prepared by mixing 80 wt-% of active material, 10 wt-% carbon black, and 10 wt-% PVDF with dimethyl sulfoxide (DMSO) solvent. The obtained slurry was coated on an aluminum-foil and dried at RT. The coated Al-foil was cut into circular pieces of 12 mm diameter (1.131 cm^2), which were then pressed with a punch of the same size at different pressure (0, 1, 2, 4, 5, 8 tons) with a hydraulic press. The electrodes (~5 mg, thickness: 50 ± 10 μm) were dried under vacuum at 120 °C overnight. Three-electrode Swagelok cells were used to study the electrochemical performance between 1.4 and 3.5 V, using metallic lithium as a counter and a reference electrode with Whatman separator and LP30 electrolyte (1 M $LiPF_6$ in ethylene carbonate (EC)/dimethylene carbonate (DMC) (1 : 1, v:v). All electrochemical measurements were done on a BioLogic VMP3 multichannel potentiostat at a constant temperature of 25 °C inside of a Binder KB240 climate chamber. Cyclic voltammetry was done at a scan rate of 1 mV s^{-1} and galvanostatic cycling with limited potential was done at a current of 5, 10, 20, 40, 80, 100, 200, 5 mA g^{-1}. Efficiency was calculated from the quotient of delithiation vs. lithiation capacity (C_{Deli}/C_{Li}).

Acknowledgments

Special thanks go to Prof. H. Ehrenberg for the opportunity to do this work in the IAM-ESS Institute, to L. Mereacre, Dr. S. Darma, U. Geckle and K. Pfeifer for help with TGA, HT-XRD and SEM measurement, as well as to Q. Fu discussing the results. This work contributes to the research performed at CELEST (Center for Electrochemical Energy Storage Ulm-Karlsruhe). The ZEISS MERLIN SEM was financially supported by the Federal Ministry of Economics and Technology based on a decision by the German Bundestag within the BMBF grant no. 03ET6017. The work also gained benefit from the beamtime allocation at PETRA-III beamlines P02.1 at DESY, Hamburg, Germany. Open access funding enabled and organized by Projekt DEAL.

Conflict of Interest

The authors declare no conflict of interest.

Keywords: cycle stability · electrode materials · lithium-ion batteries · polyoxometalate · structural water

[1] O. Renn, J. P. Marshall, *Energy Policy* **2016**, *99*, 224–232.
[2] S. Konietzko, M. Gernuks, R. Aul, E.-R. Barenschee, M. Buchert, A. Engler, C. Hoyer, W. Jenseit, M. Steinbild, F. Treffen, *Umbrella-arbeitsgr. Ressourcenverfügbarkeit* **2011**, *1*, 1–31.
[3] M. Buchert, W. Jenseit, C. Merz, D. Schüler, *Öko-Institut e.V., Freibg.* **2011**, *1*, 1–114.
[4] M. Buchert, W. Jenseit, C. Merz, D. Schüler, *Öko-Institut e.V., Freibg.* **2011**, *1*, 1–105.
[5] T. C. Wanger, *Convers. Lett.* **2011**, *4*, 202–206.
[6] D. L. Long, R. Tsunashima, L. Cronin, *Angew. Chem. Int. Ed.* **2010**, *49*, 1736–1758; *Angew. Chem.* **2010**, *122*, 1780–1803.
[7] T. Yamase, *J. Mater. Chem.* **2005**, *15*, 4773–4782.
[8] Y. V. Geletii, B. Botar, P. Kögerler, D. A. Hillesheim, D. G. Musaev, C. L. Hill, *Angew. Chem. Int. Ed.* **2008**, *47*, 3896–3899; *Angew. Chem.* **2008**, *120*, 3960–3963.
[9] A. Sartorel, M. Carraro, G. Scorrano, R. De Zorzi, S. Geremia, N. D. McDaniel, S. Bernhard, M. Bonchio, *J. Am. Chem. Soc.* **2008**, *130*, 5006–5007.
[10] R. Neumann, M. Dahan, *Nature* **1997**, *388*, 353–355.
[11] M. Genovese, K. Lian, *Curr. Opin. Solid State Mater. Sci.* **2015**, *19*, 126–137.
[12] D. E. Katsoulis, *Chem. Rev.* **1998**, *98*, 359–387.
[13] X. Luo, F. Li, B. Xu, Z. Sun, L. Xu, *J. Mater. Chem.* **2012**, *22*, 15050–15055.
[14] H. Wang, S. Hamanaka, Y. Nishimoto, S. Irle, T. Yokoyama, H. Yoshikawa, K. Awaga, *J. Am. Chem. Soc.* **2012**, *134*, 4918–4924.
[15] H. Brunner, H. Cattey, W. Meier, Y. Mugnier, A. C. Stückl, J. Wachter, R. Wanninge, M. Zabel, *Chem. Eur. J.* **2003**, *9*, 3796–3802.
[16] M. Skunik-Nuckowska, S. Dyjak, K. Grzejszczyk, N. H. Wisińska, F. Béguin, P. J. Kulesza, *Electrochim. Acta* **2018**, *282*, 533–543.
[17] V. Ruiz, J. Suárez-Guevara, P. Gomez-Romero, *Electrochem. Commun.* **2012**, *24*, 35–38.
[18] S. Dsoke, Q. Abbas, *ChemElectroChem* **2020**, *7*, 2466–2476.
[19] M. Genovese, K. Lian, *Electrochem. Commun.* **2014**, *43*, 60–62.
[20] D. P. Dubal, O. Ayyad, V. Ruiz, P. Gómez-Romero, *Chem. Soc. Rev.* **2015**, *44*, 1777–1790.
[21] J. F. Keggin, *Nature* **1933**, *131*, 908–909.
[22] J. F. Keggin, *Proc. Roy. Soc. A* **1934**, *144*, 75–100.
[23] C. E. Housecroft, A. G. Sharpe, *Inorganic Chemistry, Pearson*, **2005**.
[24] E. Coronado, C. Giménez-Saiz, C. J. Gómez-García, *Coord. Chem. Rev.* **2005**, *249*, 1776–1796.
[25] J. Fuchs, K. F. Jahr, *Z. Naturforsch. B* **1968**, *23*, 1380–1380.
[26] M. Che, M. Fournier, J. P. Launay, *J. Chem. Phys.* **1979**, *71*, 1954–1960.
[27] M. Filowitz, R. K. C. Ho, W. G. Klemperer, W. Shum, *Inorg. Chem.* **1979**, *18*, 93–103.
[28] C. Sanchez, J. Livage, J. P. Launay, M. Fournier, Y. Jeannin, *J. Am. Chem. Soc.* **1982**, *104*, 3194–3202.
[29] W. G. Klemperer, *Inorg. Synth.* **1990**, *27*, 74–85.
[30] L. A. Pérez-Maqueda, E. Matijević, *Chem. Mater.* **1998**, *10*, 1430–1435.

[31] C. C. Lin, W. H. Lin, S. C. Huang, C. W. Hu, T. Y. Chen, C. T. Hsu, H. Yang, A. Haider, Z. Lin, U. Kortz, U. Stimming, H. Y. Chen, *Adv. Mater. Interfaces* **2018**, *5*, 1–10.
[32] S. C. Huang, C. C. Lin, C. W. Hu, Y. F. Liao, T. Y. Chen, H. Y. Chen, *J. Power Sources* **2019**, *435*, 226702.
[33] S. F. Lux, I. T. Lucas, E. Pollak, S. Passerini, M. Winter, R. Kostecki, *Electrochem. Commun.* **2012**, *14*, 47–50.
[34] H. Y. Chen, R. Al-Oweini, J. Friedl, C. Y. Lee, L. Li, U. Kortz, U. Stimming, M. Srinivasan, *Nanoscale* **2015**, *7*, 7934–7941.
[35] C. Wang, C. Liu, Y. Hu, X. Bu, T. Zhao, K. Chou, Q. Li, *J. Mater. Chem. A* **2015**, *3*, 21424–21427.
[36] A. Kolary-Zurowska, A. Zurowski, S. Dsoke, B. Dembinska, S. Zoladek, M. Kiliszek, R. Marassi, P. J. Kulesza, *J. Solid State Electrochem.* **2014**, *18*, 2993–3001.
[37] A. Zurowski, A. Kolary-Zurowska, S. Dsoke, P. J. Barczuk, R. Marassi, P. J. Kulesza, *J. Electroanal. Chem.* **2010**, *649*, 238–247.
[38] A. Witkowska, S. Dsoke, R. Marassi, A. Di Cicco, *Nucl. Instrum.* **2015**, *364*, 65–69.
[39] J. B. Black, N. J. Clayden, P. L. Gai, J. D. Scott, E. M. Serwicka, J. B. Goodenough, *J. Catal.* **1987**, *106*, 1–15.
[40] D. Martel, M. Gross, *J. Solid State Electrochem.* **2007**, *11*, 421–429.
[41] W. Mei, H. Chen, J. Sun, Q. Wang, *Sustain. Energy Fuels* **2019**, *3*, 148–165.

Manuscript received: November 13, 2020
Accepted manuscript online: November 25, 2020